Debonding analysis via digital volume correlation during in-situ pull-out tests on fractal fibers

G. Jänicke, A. Vintache, B. Smaniotto, Amélie Fau, I. Farina, F. Fraternali, François Hild

Debonding analysis via digital volume correlation during in-situ pull-out tests on fractal fibers

G. Jänicke[a,b,*], A. Vintache[a], B. Smaniotto[a], A. Fau[a], I. Farina[c], F. Fraternali[d], F. Hild[a]

[a] *Université Paris-Saclay, CentraleSupélec, ENS Paris-Saclay, CNRS, LMPS – Laboratoire de Mécanique Paris-Saclay, 91190 Gif-sur-Yvette, France*
[b] *Institute of Continuum Mechanics, Leibniz Universität Hannover, 30823 Garbsen, Germany*
[c] *Department of Engineering, University of Naples Parthenope, Centro Direzionale di Napoli, Isola C4, 80143, Naples, Italy*
[d] *Department of Civil Engineering, University of Salerno, Via Giovanni Paolo II 132, 84084, Fisciano (SA), Italy*

Abstract

The quantification of debonding was performed for additively manufactured "fractal" fibers embedded within two brittle matrices. Three pull-out tests were carried out inside of an X-ray tomograph allowing for Digital Volume Correlation analyses. Relative motions at the interfaces were measured thanks to adapted meshes with split nodes. Profiles of normal, tangential and vertical displacement jumps as well as vertical strains in the fibers were used to study interfacial debonding. An articulated load transfer mechanism between the fiber and the matrix was observed in the examined tests, as demonstrated by zigzagged distributions of vertical displacement jumps and vertical strain profiles in the fibers at the initial stages of pull-out. Vertical strain concentrations were observed in correspondence to lateral protrusions (or ribs) of the reinforcing fibers. These results suggest that fiber-matrix interlocking may be affected by geometry-driven tensile stiffening effects between the ribs. For larger values of pull-out displacements, more diffuse damage of the fiber-matrix interface was observed between the ribs, especially in plaster matrices.

Keywords: Brittle matrix; Digital volume correlation; Displacement jump;

*Corresponding author
Email address: georg.jaenicke@ens-paris-saclay.fr (G. Jänicke)

Fractal geometry; Measurement uncertainty.

1. Introduction

Nature often exhibits shapes arranged according to fractal geometries and hierarchical architectures to maximize the surface area for a given volume of material [1]. For instance, fractures and joints in biological systems exhibit fractal geometries and have inspired several researchers to design optimized junctions of novel composite systems with interlocking elements [2, 3, 4]. Recent research has also investigated the use of fractal fabrics, fibers, and coatings for the reinforcement of cementitious composites (see Ref. [5] and references therein). Short and long fibers featuring complex geometries are conveniently fabricated through 3D printing techniques with polymeric and/or metallic materials [5, 6]. It is possible to additively manufacture, for instance, fibers covered by smaller-scale lattices on their lateral surfaces, as well as multiscale fabrics and coatings, cross-sections, or junctions/embossments of fibers with hierarchical mesostructures. Alternatively, one may employ nanoscale coating and/or plasma irradiation techniques to manufacture reinforcing elements with multiscale patterns [7, 8, 9, 10]. Such reinforcements are combined with different matrices to improve the bond strength of the reinforcing component and the overall fracture toughness of the composite material. It is expected that a thin layer of the matrix will cover the multiscale surface of fractal reinforcements, thereby causing drastic improvements in interfacial bonding during the pull-out of such composites.

Pull-out tests are one of the experimental routes to characterize debonding at an elementary level [11, 12, 13, 14, 15]. Such tests are challenging since most phenomena are hidden inside tested samples [15] or the geometries are modified [12, 13]. To by-pass such limitations, Computed Tomography (CT) may be considered. It allows the material bulk to be imaged in a nondestructive way [16]. Further, when such samples are loaded in-situ [17], deformed configurations can be imaged when the mechanical load is applied. With such

data sets, it then becomes possible to register these volumes to measure 3D displacement fields via digital volume correlation (DVC) [18, 19, 20]. In-situ pull-out tests were performed on a traditional reinforcing bar surrounded by a concrete cylinder [21], and analyzed qualitatively, particularly for understanding the cracking pattern resulting from the pull-out failure. Post-mortem CT scans were proposed to visualize air voids after failure [22]. The magnitude of the debond area was not quantified. The analysis of in-situ tests on steel fibers, in particular hooked-end, was studied thanks to local DVC [23]. The strain field in the concrete matrix surrounding the fiber was successfully evaluated to better understand pull-out failure. Yet no information was given about the interfacial behavior.

The present study aimed to extract quantitative interfacial data in a pull-out test on a matrix composed of mortar or plaster and a metallic fiber. The study focused on the very early stages of debonding (*i.e.*, close to the ultimate load the system was able to carry). Such analysis calls for the measurement of displacement jumps at interfaces. Such approach was made possible thanks to finite-element(FE)-based DVC in which meshes can be tailored to the local morphology of various phases [24, 25]. Regarding the experimental setup used in this work, a testing machine located inside an X-ray tomograph was used to image the loaded sample in-situ. A common challenge of frictional cracks is that they cannot be detected on the volumes by standard image analyses based on gray level variations. Conversely, DVC analyses may quantify the presence of cracks, whether they are open or in frictional conditions [26].

In the following, regularized DVC was used since, apart from the interfaces, the underlying behavior of the matrix and the fiber was assumed to be linear elastic [27]. The considered meshes were constructed using the marked gray level contrast between the fiber and the surrounding matrix. Nodes were split at the interface to measure displacement jumps and analyze the debonding mechanism for load levels close to the ultimate point. To quantify crack openings, measurement uncertainties were needed. Two so-called "repeat-scans" were acquired under similar conditions to have access to displacement jump and strain uncer-

tainties. Theoretical and technical basics are explained, and the experimental setup and procedure are exposed in Section 2. Section 3 deals with DVC results and contains a discussion of displacements and residuals at different levels of loading. In Section 4, debonding effects at the interface between the fiber and the matrix while performing pull-out tests, also taking measurement uncertainties into account, are analyzed.

2. Material and Methods

A dedicated experimental setup and protocol, as well as DVC mesh and regularization, were specifically designed for analyzing debonding during in-situ pull-out tests on brittle matrices.

2.1. Material and Specimen

Additively manufactured reinforcing fibers were fabricated through Electron Beam Melting (EBM) employing an Arcam EBM Q20 plus facility. The "fractal" geometry was made of a titanium alloy (Ti6Al4V). The fiber surface was derived from nature regarding its hierarchical design. The result was expected to lead to a strong connection between the fiber and the surrounding matrices (*i.e.*, enhanced interfacial shear strength). Figure 1(a) shows the morphological features of several "fractal" fibers with different geometries. A hierarchical organization was achieved by a fractal algorithm based on the Koch curve and three complexity parameters n, m and p to generate the cross-section and vertical profile of reinforcing elements [5]. The parameter n indicates the number of self-similar subdivisions of the base Koch triangle on the cross-section of the fiber; m counts the analog number of subdivisions of that triangle along a base segment of the longitudinal profile; and p gives the number of copies of the base segment along the span of the fiber. The higher such parameters, the higher the complexity of the fiber [Figure 1(b)].

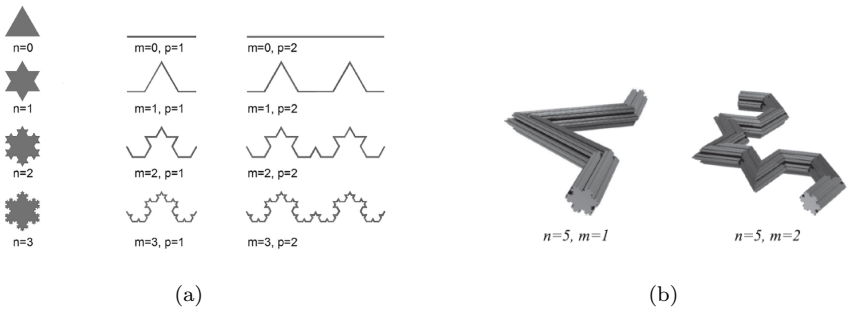

Figure 1: "Fractal" fibers (reproduced with permission from Ref. [5]). (a) Sections of "fractal" fibers. (b) Examples of fibers with "fractal" sections

Mortar and plaster matrices reinforced with fractal fibers were fabricated to be mechanically investigated. The mortar mixes were prepared using fly ash (50%wt), blast furnace slag (20%wt) as sand replacement, and the remaining natural aggregates were used in the fine fraction (0/4 mm). An ordinary Portland cement (OPC) with 0.5 W/C ratio was employed to prepare cylindrical specimens, which were cast in two steps in 36 mm $\times$ 75 mm PVC molds made of 3D printed polylactide (PLA). First, the reinforcing fiber was centered in the mold base, and then mortar was poured until the mold was filled. The specimens were cured within the molds at room temperature for 24 h, and for an additional 27 days at room temperature with no mold before testing. The same procedure was used to prepare plaster samples using commercial plaster. It was mixed with clean water using a water/plaster (W/P) ratio equal to 0.66.

Three samples with fractal fiber embedded in a brittle matrix were tested in-situ. The examined fiber had a diameter of 7 mm, complexity parameters $n = 1$, $m = 1$, $p = 3$, and a matrix-embedded length of 6.5 cm [Figure 2(a)]. Sample M1 had a mortar matrix [Figure 2(b)], whereas samples P1 and P2 comprised a plaster matrix [Figure 2(c)]. The analysis of samples P1 and P2 will probe the repeatability of the debonding process. The three samples had similar geometries with an external diameter of 36 mm and a height of 75 mm. The fibers had a diameter of 7 mm and the following geometric parameters: $n = 5$, $m = 1$ and $p = 6$. The cylindrical shaft on the top of the fiber was

drilled (bore 6 mm in diameter) before testing for load application purposes [Figure 3(b)].

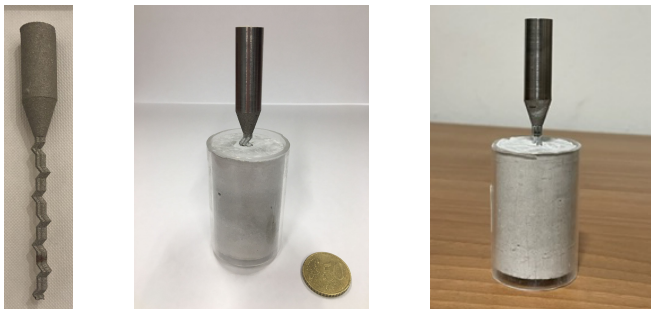

(a) (b) (c)

Figure 2: Examined fiber (a). Two of the to-be tested samples: M1 with a mortar matrix (b), and P1 with a plaster matrix (c)

2.2. Experimental analysis

In-situ tests were performed with a tension-compression testing machine [Figure 3(a)] inside the X-ray tomograph of LMPS. Consequently, the components for performing the pull-out test must not obscure the X-ray beam at any angular position. The setup specifically designed for this application is detailed in Figure 3(b). It consists of two 3D-printed Acrylonitrile-butadiene-styrene (ABS) components clamping the sample for the pull-out test. The upper ABS component clamps the shaft of the fiber with a pin. The lower ABS component encases the sample and compresses the cylindrical matrix with a rubber ring between the surfaces equalizing the uneven upper surface roughness of the samples [Figure 3(b-c)]. The upper part of the fiber at the exterior of the matrix was drilled to fit in a pin. The two ABS components were screwed on the upper and lower platens of the testing machine while the sample was located in the interior of the lower component.

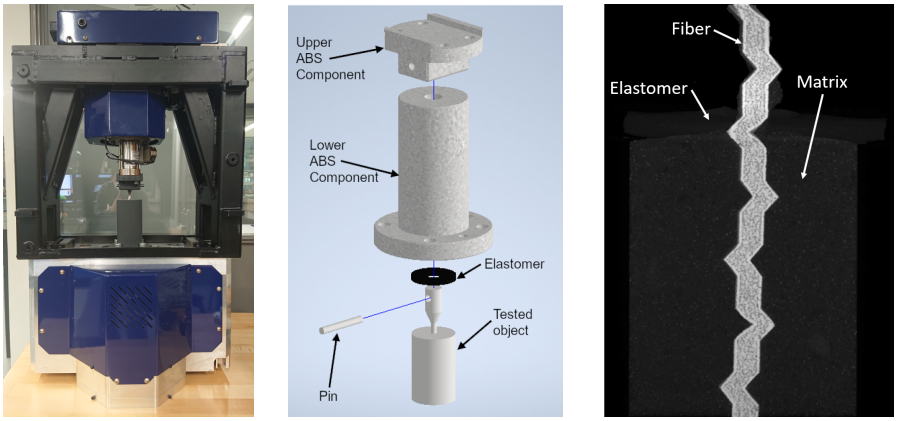

(a) (b) (c)

Figure 3: Experimental setup. (a) Testing machine and pull-out setup. (b) Components for pull-out setup. (c) Sagittal section of sample P2 for scan 0

The three in-situ tests consisted of successive stages where the displacement was increased and then the sample was scanned while maintaining the applied load. Each CT scan was based on 1,000 projections and lasted about 20 min. All hardware parameters used for CT imaging are given in Table 2 (in the appendix).

The sequences of loading steps and scans for samples M1, P1 and P2 are shown in Figure 4(a-c), respectively. They are indicated with respect to the pull-out curve displaying the applied force F as a function of the actuator stroke s for each test. The three in-situ tests began with an initial "pre-load" of 50 N. Afterward, a first CT scan of the sample was performed (scan 0), followed by a second scan at the same load with a slight lateral displacement of the whole testing machine (scan 01). The second scan was considered as a "repeat scan", subsequently used to evaluate measurement uncertainties for each test. Then, a pull-out displacement was applied with a speed of 10 µm/s. For sample M1, three scans (02, 03 and 04) were performed before sudden and fatal fiber failure. For samples P1 and P2, fiber damage occurred after scan 03 (at ca. 700 N for test P1, and ca. 1000 N for test P2), which induced load drops. The loading

was then interrupted, and another CT scan was acquired (scan 04) at a stable force for both cases, followed by another stroke increment of 0.3 mm, and the last scan (05) for P2. For P1, several smaller stroke increments were applied and a series of five scans (04, 05, 06, 07 and 08) were acquired to investigate the pull-out behavior after fiber damage. When continuing to increase the stroke after these scans, final failure of the fiber took place. Thus, a series of five scans was acquired to characterize fiber pull-out for sample M1, and a series of nine and six scans for samples P1 and P2, respectively. It can be noted that each of them was performed after a small dwell to mitigate relaxation effects.

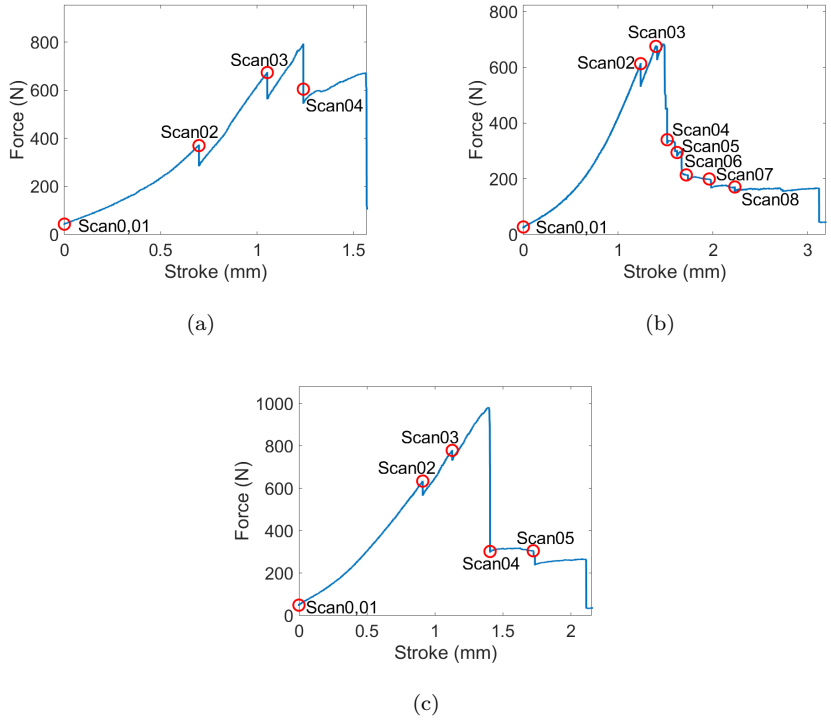

Figure 4: Pull-out curves for samples M1 (a), P1 (b) and P2 (c)

2.3. Mesostructure Segmentation and Microstructure-Based Mesh

For performing an accurate analysis of the interfacial behavior, the mesostructure was meshed with a precise description of the interface. The significant con-

trast observed in Figure 3(c) was employed for segmenting the reconstructed volume of the reference configuration and distinguishing the fiber from the matrix. Nodes were placed on the interface to fit closely the fiber shape, and individual meshes associated with the fiber and the matrix were designed separately using Avizo Fire 8 (the interface nodes of the fiber are visualized in green in Figure 5). For sample P2, 449 nodes depict the top surface of the matrix that was in contact with the elastomeric ring. The global mesh was made of 22,623 three-dimensional tetrahedra (T4) with a mean size defined as the cube root of the mean volume of the T4 elements of 26 voxels (4,165 elements for the fiber with a mean element size of 13 voxels, and 18,458 elements for the matrix with a mean element size of 28 voxels). Fiber and matrix meshes can be used separately representing 14,505 degrees of freedom including the relative displacement between them at the interface.

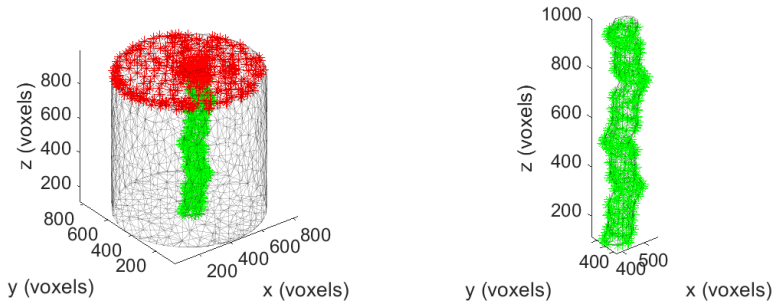

(a) (b)

Figure 5: Mesh of tested sample (a) and fiber (b) with split nodes at the interface marked in green. The top surface nodes marked in red were in contact with the elastomeric ring of the setup [Figure 3(b)]

2.4. Regularized DVC

The DVC analysis of the in-situ test is based on the assumption of gray level conservation between two images

$$f(\mathbf{x}) = g(\mathbf{x} + \mathbf{u}(\mathbf{x})), \tag{1}$$

where f are the gray levels of the discrete voxel positions $\mathbf{x}$, and g the gray level image where a displacement $\mathbf{u}$ occurred. The residual denoted ρ is equal to the absolute difference between the gray level images f and g once registered

$$\rho(\mathbf{x}) = |f(\mathbf{x}) - g(\mathbf{x} + \mathbf{u}(\mathbf{x}))|. \tag{2}$$

Thus, the measured displacement field is determined from the minimization of the cost function Ψ^2

$$\mathbf{u}_{meas} = \arg\min(\Psi^2(\mathbf{u})), \tag{3}$$

where $\Psi^2(\mathbf{u})$ is defined as the squared L_2 norm of $\rho(\mathbf{x})$ computed over the region of interest (ROI)

$$\Psi^2(\mathbf{u}) = \sum_{\text{ROI}} \rho^2(\mathbf{x}). \tag{4}$$

In the present case, the displacement field is decomposed over a kinematic basis made of the shape functions of the underlying T4 discretization

$$\mathbf{u}(\mathbf{x}) = \sum_i \upsilon_i \mathbf{N}_i(\mathbf{x}) \tag{5}$$

where υ_i denotes the nodal displacement associated with the i-th shape function $\mathbf{N}_i$. The unknowns to be determined then become the nodal displacements that are gathered in the column vector $\{\boldsymbol{\upsilon}\}$, and Ψ^2 is minimized globally by considering all voxels of the ROI. The DVC algorithm iteratively searches for the minimum of the global residual until reaching a convergence criterion written in terms of the corrections to $\{\boldsymbol{\upsilon}\}$. The residuals are small if the DVC calculation was able to find a suited solution, whereas cracks or unresolved deformations result in higher residuals [26].

In the present analyses, regularized DVC was selected [27, 28]. It consists in penalizing the previous cost function with a mechanics-based cost function, which is derived from the global equilibrium in an FE sense considering an elastic analysis

$$[\mathbf{K}]\{\boldsymbol{\upsilon}\} = \{\mathbf{f}\} \tag{6}$$

where $[\mathbf{K}]$ is the stiffness matrix, and $\{\mathbf{f}\}$ the nodal force vector. Since the calculation of $\{\boldsymbol{\upsilon}_{meas}\}$ does not satisfy equilibrium, residual forces $\{\mathbf{f_{res}}\}$ remain

$$\{\mathbf{f_{res}}\} = [\mathbf{K}]\{\boldsymbol{v}_{\mathbf{meas}}\} - \{\mathbf{f}\}. \tag{7}$$

The nodal forces in the bulk are equal to 0 in the absence of body forces leading to

$$\{\mathbf{f_{res}}\} = [\mathbf{K}]\{\boldsymbol{v}_{\mathbf{meas}}\} \tag{8}$$

and its L_2 norm leads to the equilibrium gap Φ^2

$$\Phi^2(\{\boldsymbol{v}\}) = \{\boldsymbol{v}\}^\top [\mathbf{K}_B]^\top [\mathbf{K}_B]\{\boldsymbol{v}\} \tag{9}$$

where $[\mathbf{K}_B]$ is the partial stiffness matrix associated with bulk nodes.

In the following, an independent regularization at the interface and at other external nodes is considered. A penalization of fluctuations of nodal forces at the interface is taken into consideration. Two cost are taken into account to prevent rapid variations of tractions [28] at the interface. Distinguishing between bulk (B), so-called Neumann (N) and Dirichlet (D) degrees of freedom (DOFs) leads to an identity matrix $[\mathbf{I}]$ depending on the corresponding projection matrices $[\mathbf{D}]$

$$[\mathbf{I}] = [\mathbf{D}_B] + [\mathbf{D}_N] + [\mathbf{D}_D] \tag{10}$$

the partial stiffness matrix reads

$$[\mathbf{K}_m] = ([\mathbf{D}_B] + [\mathbf{D}_N])[\mathbf{K}] \tag{11}$$

and the equilibrium gap functional

$$\Phi^2_m(\{\boldsymbol{v}\}) = \{\boldsymbol{v}\}^\top [\mathbf{K}_m]^\top [\mathbf{K}_m]\{\boldsymbol{v}\} \tag{12}$$

is considered for bulk and Neumann DOFs. In a similar way, the partial stiffness matrix corresponding to the Dirichlet DOFs (*i.e.*, consisting of interfacial and top surface DOFs in the presence case, see Figure 5) reduces to

$$[\mathbf{K}_D] = [\mathbf{D}_D][\mathbf{K}] \tag{13}$$

and the corresponding penalty term for Dirichlet DOFs

$$\Phi^2_D(\{\boldsymbol{v}\}) = \{\boldsymbol{v}\}^\top [\mathbf{K}_D]^\top [\mathbf{L}][\mathbf{K}_D]\{\boldsymbol{v}\} \tag{14}$$

where [**L**] corresponds to the discrete Laplace-Beltrami operator [29]. Taking into account all three cost functions leads to the minimization of their weighted sum

$$\{\mathbf{u}\}_{meas}^{reg} = \arg\min(\Psi^2(\{\boldsymbol{v}\}) + w_m\Phi_m^2(\{\boldsymbol{v}\}) + w_c\Phi_D^2(\{\boldsymbol{v}\})) \tag{15}$$

where w_m and w_c are the corresponding weights, which are proportional to regularization lengths ℓ_m and ℓ_D raised to the power 4 [30].

The reconstructed volumes were registered using the Correli 3.0 framework [31]. Table 3 (in the appendix) gathers further details concerning the DVC analysis parameters. The mechanical regularization length of the DVC calculations was set to 50 vx on all bulk and Neumann DOFs, and to $50\sqrt{2}$ vx on all other DOFs. These lengths were close to that of the elements.

2.5. Debonding Measurement

The measured displacement fields $\mathbf{u}_{meas}^{reg}$ were dominated by rigid body motions $\mathbf{u}_{RBM}$ due to tilt induced by the elastomer while the loading was applied [Figure 3(b-c)]. For instance, Figure 6(a) shows the vertical displacement field for scan 03 of sample P2. Thus, a rigid body motion compensation was performed to visualize "mechanical" displacement fields $\mathbf{U}$

$$\mathbf{u}_{meas}^{reg} = \mathbf{u}_{RBM} + \mathbf{U}. \tag{16}$$

The compensated vertical displacement field corresponding to the raw field [Figure 6(a)] is displayed in Figure 6(b). The mechanical response of the sample appears more clearly, with a significant interfacial displacement jump between the fiber and the matrix on the top surface. In the following, only results with compensated displacement fields are shown and discussed.

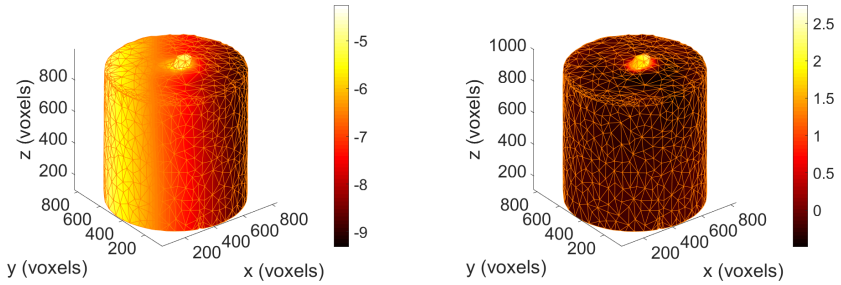

(a) (b)

Figure 6: Displacement field of sample P2 in the vertical direction for scan 03 without (a) and with (b) rigid body motion compensation

The quantity of interest for debonding analyses is the displacement jump at the interface of the two constituents, which is defined as

$$d\mathbf{U} = \mathbf{U}_{fiber} - \mathbf{U}_{matrix}. \tag{17}$$

For a detailed analysis of the effects at the interface between the fiber and the brittle matrices, a separation in terms of normal and tangential components is written for each interfacial node pair

$$d\mathbf{U} = dU_n\,\mathbf{n} + d\mathbf{U_t} \tag{18}$$

where dU_n is the displacement jump along the normal of the considered interfacial node $\mathbf{n}$, and $d\mathbf{U_t}$ the corresponding tangential component. Figure 7 shows the definition of displacement jumps components at the interface of the two constituents. Interpenetration of the two phases may occur when the normal component becomes negative.

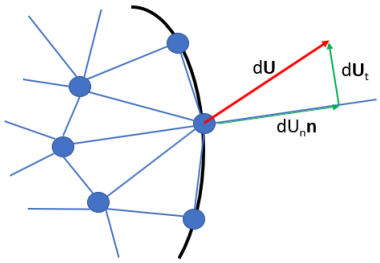

Figure 7: Decomposition of the displacement jump vector $d\mathbf{U}$ into normal dU_n and tangential $d\mathbf{U_t}$ components

2.6. Uncertainty Quantification

To entirely describe a measurement result, uncertainties have to be taken into consideration [32]. So-called "repeat scans" during which the tested sample was imaged two times under similar mechanical conditions served for the quantification of measurement uncertainties. Between these repeat scans, the loading was not changed but the testing machine (and thus the sample) was moved in the tomograph by about 20 pixels (*i.e.*, ca. 0.9 mm). Due to spurious displacements while rotating the sample, detector noise, and other random errors, the reconstructed volumes are different for any new acquisition. As a consequence, displacement uncertainties arise due to the previous causes in addition to DVC algorithms.

Only significant values of displacement jumps are considered as a criterion for characterizing debonding between the matrix and the fiber. Thus, a threshold had to be chosen to differentiate between results that are lower or higher than the measurement uncertainty for any quantity of interest. The detection threshold was defined as k times the standard displacement uncertainty evaluated by registering the repeat scan with the reference scan [33]. In Table 1, the standard displacement uncertainties are reported for the three displacement jump components that are commented in the sequel. For sample M1, the uncertainty levels were higher than those of the other two specimens. Yet the strain uncertainty remained of the same order as the other two cases. The detection threshold ranged from 0.05 to 0.55 vx (*i.e.*, from 2.3 to 25 µm), depending on

the considered sample and displacement jump component (Table 1). The standard strain uncertainty was the lowest for sample P1. In all cases, it was less than 10^{-3}. Such level could be achieved thanks to the regularization scheme used herein.

The value of k was selected in such a way that virtually all nodes were deemed bonded in the repeat scans (see first sub-figures of Section 4). In the following analyses, the value $k = 5$ was selected, which is a compromise between avoiding false alarms (*e.g.*, detecting debonded nodes in the repeat scans) and excluding nodes that are actually debonded (in subsequent scans).

Table 1: Standard measurement uncertainties and ratio k used in the detection threshold for the three in-situ tests

Test	M1	P1	P2
σ_{dU_n} (vx)	0.04	0.01	0.02
σ_{dU_t} (vx)	0.11	0.03	0.07
σ_{dU_z} (vx)	0.05	0.03	0.04
k	5	5	5
$\sigma_{\epsilon_{zz}}$	8×10^{-4}	2×10^{-4}	8×10^{-4}

3. DVC Results and discussion

This section deals with the results of DVC calculations serving for the analysis of interfacial effects during the pull-out tests. Displacements and residuals are shown in the sequel.

3.1. Measured Displacement Fields

Displacement fields in the vertical direction (*i.e.*, U_z) for scans 03 of each test are shown in Figure 8. In all three cases, displacements of the order of a few voxels occurred at the upper location of the fiber, while no significant displacements were observed in the matrix. Differences between the three cases are noted as to the amplitude of displacements.

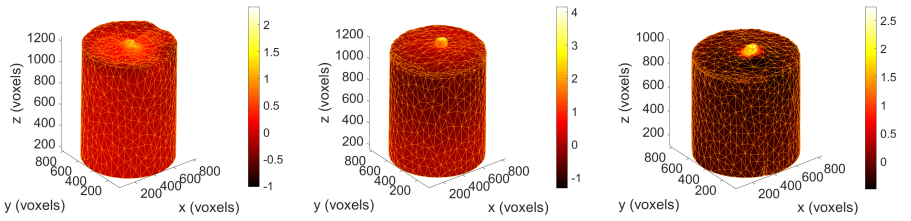

Figure 8: Displacement fields in vertical direction of scan 03 for sample M1 (a), P1 (b) and P2 (c)

The key information is the evolution of displacements within the tested samples. Figure 9 shows the norm of displacement fields of sample P2 at different heights for two different scans. Figure 9(a) displays the displacement norm computed for (repeat) scan 01 at the height $z = 650$ vx, which is about two thirds of the total height. The same field is shown for $z = 850$ vx, which is closer to the top surface, in Figure 9(b). No significant displacements are observed with the selected range. Figures 9(c,d) correspond to the displacement norm for scan 03 (*i.e.*, last scan prior to the ultimate force) for the same sections. The displacement amplitudes are significantly higher in the fiber, while the nodes belonging to the matrix experienced very low displacements once corrected. The magnitude of displacements at the position of the fiber is up to 1.5 vx at the top part of the sample. Figure 9(c) shows that displacement jumps also occurred at lower heights of the sample P2.

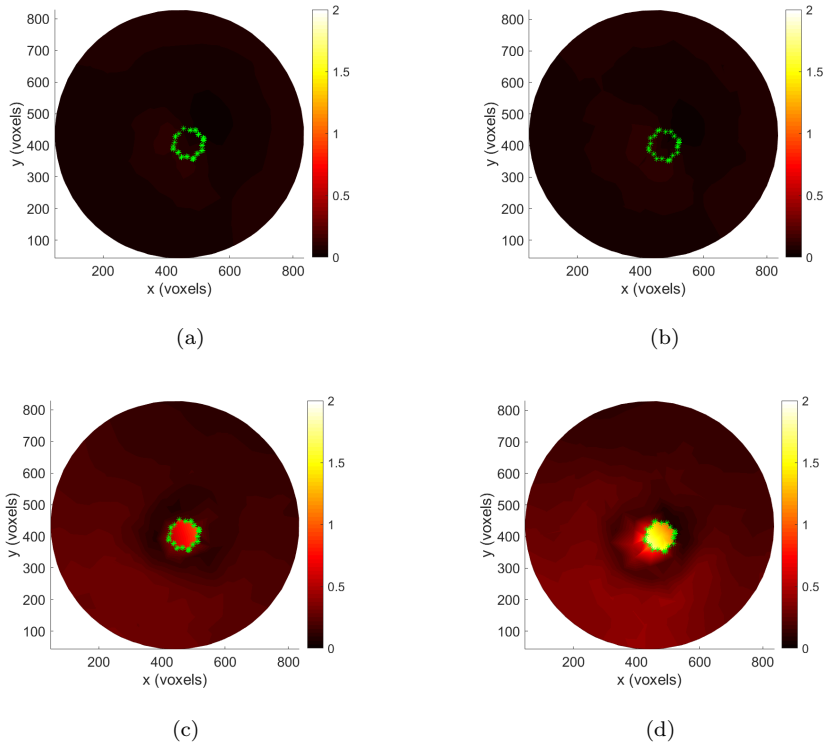

Figure 9: Norm of the displacements $||\mathbf{U}||$ (expressed in voxels) for sample P2. $x-y$ sections of scan 01 for $z = 650$ vx (a) and $z = 850$ vx (b). $x-y$ sections of scan 03 for $z = 650$ vx (c) and $z = 850$ vx (d). The nodes belonging to the interface are represented in green.

3.2. Analysis of Residuals

The nodal gray level residuals at $z = 850$ vx for scans 01 and 03 of sample P2 are shown in Figure 10. For both scans, their value is of the order of 3 gray levels for the matrix, whereas they reached ca. 7 gray levels within the fiber. The fact that the gray level residuals remained rather small, and very close for both scans, allowed us to deem the DVC registrations successful. It is believed that the residuals are a signature of small gray level variations during the experiment.

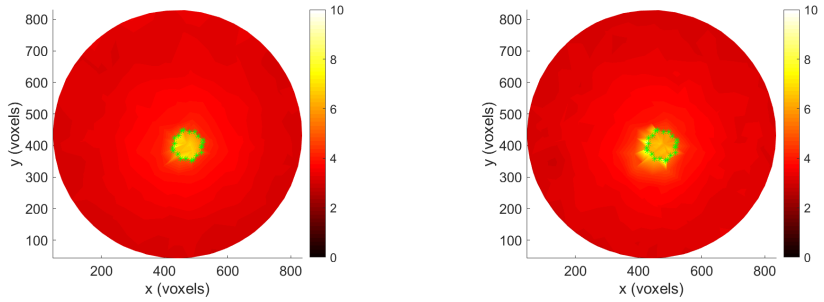

(a) (b)

Figure 10: Nodal gray level residuals for sample P2. $x-y$ sections for scans 01 (a) and 03 (b) for $z = 850$ vx. The nodes belonging to the interface are depicted in green.

Considering bulk and Neumann nodes, the residual forces, which should be equal to 0 in the present case (see Section 2.4), read

$$\{\mathbf{f}_{res}\} = [\mathbf{K}]\{\mathbf{u}^{reg}_{meas}\}, \tag{19}$$

small $\{\mathbf{f}_{res}\}$ values correspond to low equilibrium residuals. Figures 11(a,b) show the norm of equilibrium residuals $\|\{\mathbf{f}_{res}\}\|$ and their vertical component at section $z = 850$ vx for scan 01 of sample P2. The vertical component as well as the norm are very close to 0. For scan 03, similar plots are shown in Figure 11(c,d). The residuals are higher, reaching a level of 10 arbitrary units close to the interface. This observation may indicate that damage occurred in the matrix. It appears in Figure 11(d) that the main direction of equilibrium residuals was vertical with values reaching an extent of 10 arbitrary units as well.

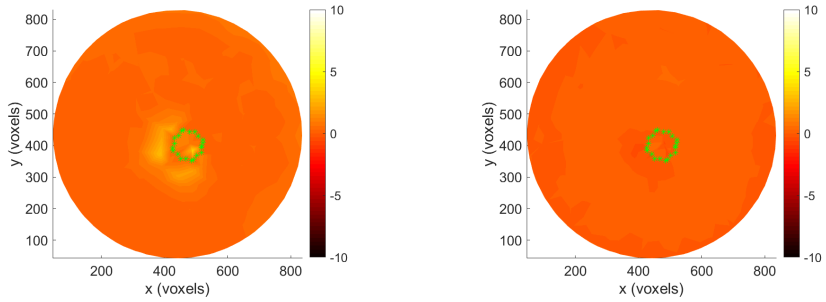

(a)

(b)

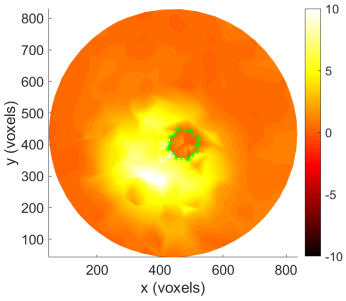

(c)

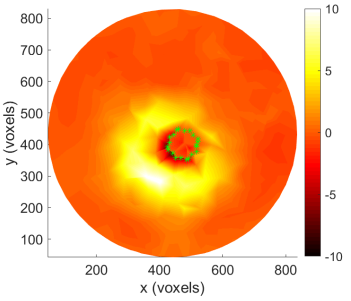

(d)

Figure 11: Equilibrium residuals (in arbitrary units) for sample P2 when $z = 850$ vx. Norm (a) and z-component (b) for scan 01, and (c,d) for scan 03, respectively. The nodes belonging to the interface are shown in green.

4. Debonding Analysis

The previously measured displacement fields were post-processed to assess the interfacial displacement jumps, which serve for the analysis of interfacial effects during the three tests. The detection threshold (*i.e.*, $k = 5$) was selected according to the uncertainty quantification performed in Section 2.6.

4.1. Test M1

Figure 12 displays the profiles of normal displacement jumps during the in-situ test on sample M1. For the first scan, the displacement jump of very

few points exceeded the detection threshold. For the second scan, which corresponded to an applied force of 50% of the ultimate load [Figure 4(a)], the fraction of nodes whose displacement jump was greater than the detection threshold was less than 1%. The same observation applied to the third scan (*i.e.*, less than 1% of the nodes had a displacement jump greater than the detection threshold). At this load level (*i.e.*, 85% of the ultimate load), interlocking was still fully active. For the last scan, the top fifth of the fiber had displacement jumps greater than the detection threshold, which represented only 4% of the total number of nodes. Yet, the displacement jump amplitudes remained very limited (*i.e.*, less than 0.5 vx or 23 µm). Even beyond the ultimate load, the levels of normal displacement jumps remained very limited. The debond zone was mostly concentrated in the first "protrusion" [*i.e.*, the region where the fiber was not aligned with the loading direction, see Figure 12(d)].

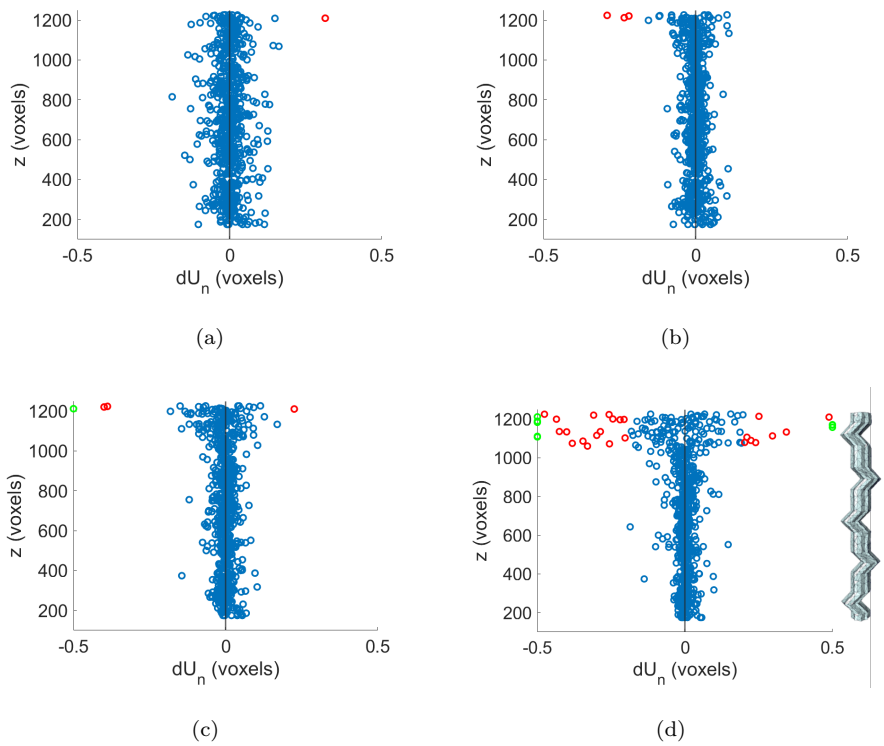

Figure 12: Normal displacement jump as a function of vertical nodal position of scans 01 (a), 02 (b), 03 (c) and 04 (d) of sample M1. Values below the detection threshold are shown in blue and above in red. Data whose level does not lie within the selected range are shown with a saturated value in green.

In Figure 13, the profiles of tangential displacement jumps are reported for the four analyzed scans. For the first scan, the displacement jump uncertainties were the highest of all analyzed cases (see Figures 17(a) and 21(a)). This trend may be due to the fact that the contrast in the mortar matrix was lower than that of plaster, which contained more porosities. For the second scan, debonding occurred over about 10% of the fiber height. The fraction of nodes whose displacement jump was greater than the detection threshold was equal to 1%. This level increased to 3% for the third scan. Yet the extension of the debond zone remained very limited. For the last scan, debonding still developed a bit (over about 20% of the total height of the fiber), even though the applied

load was lower than its ultimate level. The fraction of nodes whose displacement jump was greater than the detection threshold was equal to 14%, which is higher than the corresponding fraction for the normal component.

When analyzing both displacement jump components, it is concluded that interlocking was very strong in experiment M1. The existence of this mechanism is evidenced by the fact that the magnitude of normal displacement jumps remained very small, and was accompanied by limited tangential displacement jumps. As a consequence, debonding was confined to the very top part of the fiber (*i.e.*, first protrusion, see Figures 12(d) and 13(d)]] and did not develop significantly, contrary to the two experiments on plaster (see below).

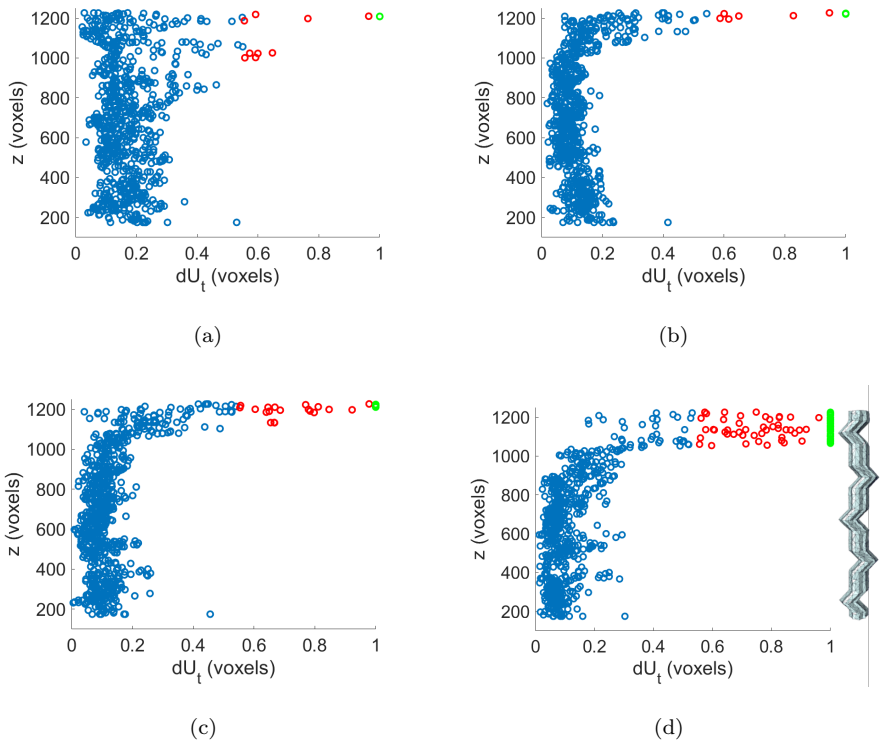

Figure 13: Norm of tangential displacement jump as a function of vertical nodal position of scans 01 (a), 02 (b), 03 (c) and 04 (d) of sample M1. Values below the detection threshold are shown in blue and above in red. Data whose level does not lie within the selected range are shown with a saturated value in green.

For the vertical displacement jump profiles (Figure 14), it is observed that debonding had already initiated for the second scan (*i.e.*, for an applied force of about 50% of the ultimate load) for the top 20% part of the fiber. The fraction of nodes whose displacement jump was greater than the detection threshold was equal to 4%. The amplitudes of the displacement jumps increased a bit for the third scan. The fraction of nodes whose displacement jump was greater than the detection threshold was equal to 7%. For the last scan, the displacement jump amplitudes did not decrease, even though the applied force decreased a bit. The fraction of nodes whose displacement jump was greater than the detection threshold was equal to 16%, namely, higher than for the previous scan. This level was very close to that associated with the tangential component.

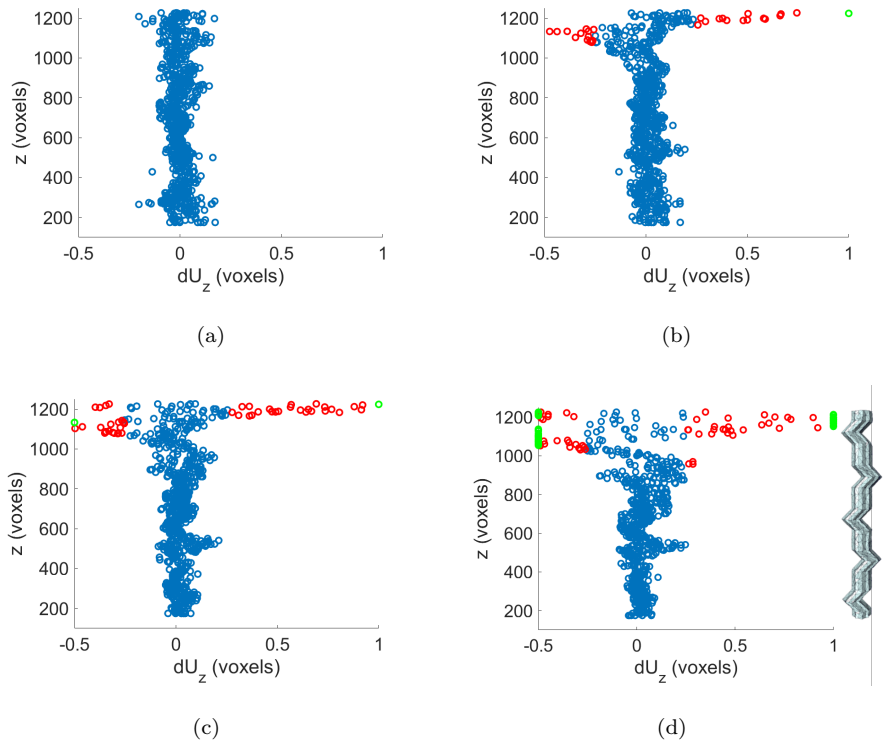

Figure 14: Vertical displacement jump as a function of vertical nodal position of scans 01 (a), 02 (b), 03 (c) and 04 (d) of sample M1. Values below the detection threshold are shown in blue and above in red. Data whose level does not lie within the selected range are shown with a saturated value in green.

With the constructed mesh in which the matrix and the fibers were meshed consistently (Figure 5), it was possible to analyze the profiles of vertical strains ϵ_{zz} in the fiber. Since T4 elements were used, the strains are uniform in each element. In Figure 15, the vertical strains are plotted with respect to the vertical position z of the center of mass of each element. To make the analysis easier, red lines are drawn and correspond to k-point mean values (*i.e.*, calculated over a sliding window of length $k = 100$ vx) across neighboring points of the centers of mass of each element. For scan 01, the vertical strains fluctuated along the vertical direction, which are assumed to be due to the fiber geometry. Even though spatial correlations arose, the standard strain uncertainty remained

less than 10^{-3} (Table 1). For scan 02, the strain levels remained small, even though some vertical fluctuations (different from the previous ones), were again observed. This observation proves that the strain fluctuations observed for scan 02 are not dominated by measurement uncertainties. They became more prominent for scan 03 essentially at the same locations as for scan 02. For scan 04, there was a highly strained zone that appeared on the top part of the fiber, which was bent and became a plastic hinge [Figure 15(d)]. This zone is where fracture eventually occurred. It coincided with the zone where debonding was observed (Figure 14).

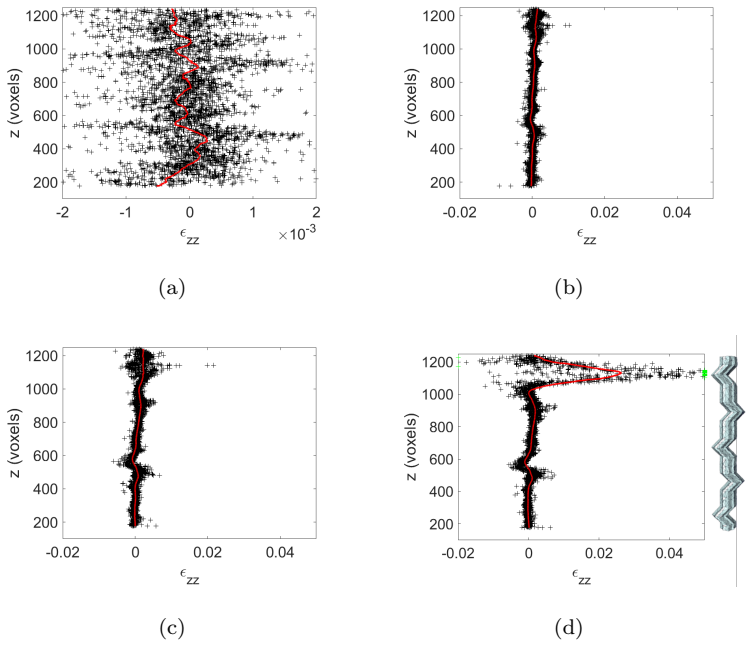

Figure 15: Vertical strain in the fiber ϵ_{zz} as a function of vertical position of element center of gravity z for scans 01 (a), 02 (b), 03 (c) and 04 (d) of sample M1. The red line depicts the k-point mean values (with $k = 100$ vx). Data whose level does not lie within the selected range are shown with a saturated value in green.

It is interesting to note that the three sets of displacement jump data enabled complementary information to be extracted from the pull-out test on a mortar matrix. The extend of debonding was best observed on the vertical and

tangential components. Given the geometry of the fiber, this first data set was not sufficient to fully analyze the pull-out test. With the normal displacement jump component, it was shown that interlocking was active throughout most of the test over a very significant part of the fiber height. As a consequence, the tangential displacement jumps remained very limited in magnitude. Further, the fact that the displacement jump amplitudes after the peak load remained very close to those observed close to the peak is an additional indication that interlocking was very strong and prevented reverse motions to take place. Last, the analysis of the vertical strain profiles in the fiber showed that bending occurred in some part of the fiber, and the strains concentrated in the zone that eventually failed.

4.2. Test P1

The second in-situ test consisted in pulling out the same fiber from a plaster matrix, which was expected to be weaker than the previous (mortar) matrix. Figure 16 shows the normal displacement jump profile along the vertical direction. For the first scan, which was used for assessing the measurement uncertainties, virtually no measurement point (*i.e.*, less than 1%) exceeded the selected detection threshold. For the second scan, which corresponded to an applied force of 600 N [Figure 4(b)], there was a clear crack opening/closure activity in the upper half of the fiber. The fraction of nodes whose displacement jump was greater than the detection threshold was equal to 14%. The fact that there were positive and negative displacement jumps is believed to be due to the specific geometry of the fiber and that the interface was not perfect.

For the third scan (*i.e.*, $F = 700$ N), the nodes with displacement jump amplitudes greater than the detection threshold were distributed all over the fiber height. Conversely, there still were numerous nodes whose displacement jumps were lower than the measurement uncertainty. This observation shows that interlocking occurred all over the fiber. The fraction of nodes whose displacement jump was amplitude greater than the detection threshold was equal to 53%. It is worth noting that the applied force only slightly increased between

the second and third scans. Yet, there was a significant difference in terms of distribution of displacement jumps.

For the last five scans, the normal displacement jump profiles were very similar. This was due to the fact that the applied force was of the same order of magnitude (*i.e.*, 250 ± 70 N). The displacement jump activity concentrated essentially in the upper quarter of the fiber. Yet there other locations ("hot spots") where debonding occurred. These zones are essentially located in vertical parts of the fiber. This observation is explained by tearing effects due to the progressive pull-out of the fiber. The fraction of nodes whose displacement jump was greater than the detection threshold was essentially the same (*i.e.*, equal to 23%, 21%, 22%, 22%, 24%, respectively) even the applied decreased from 320 N to 180 N.

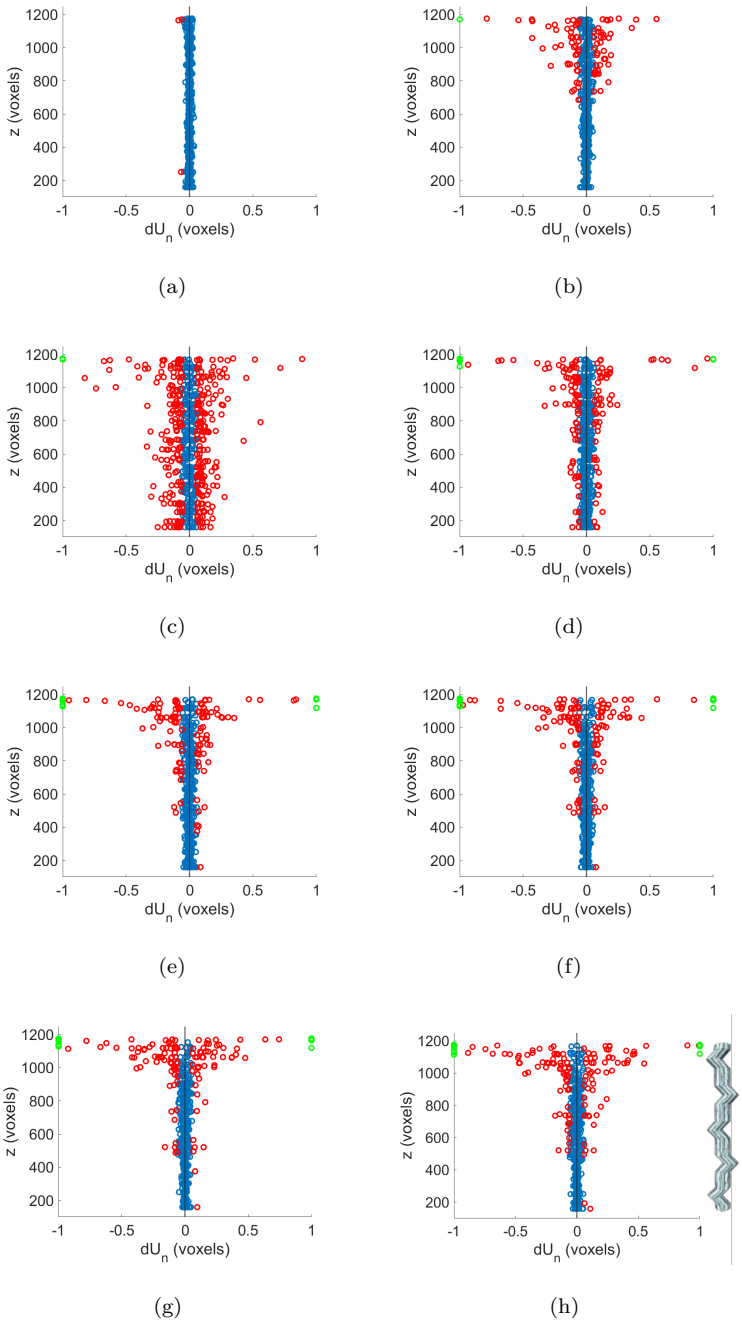

Figure 16: Normal displacement jump as a function of vertical nodal position of scans 01 (a), 02 (b), 03 (c), 04 (d), 05 (e), 06 (f), 07 (g) and 08 (h) of sample P1. Values below the detection threshold are shown in blue and above in red. Data whose level does not lie within the selected range are shown with a saturated value in green.

In Figure 17, the norm of the tangential displacement jumps is displayed as a function of the vertical coordinate. For the first scan, as in the previous case, very few nodes (*i.e.*, 2%) had a displacement jump amplitude greater than the selected detection threshold. For the second scan, about one half of the fiber experienced significant displacement jumps. In addition, there were some hot spots essentially located in vertical parts of the fiber. The fraction of nodes whose displacement jump was greater than the detection threshold was equal to 43%. It is worth mentioning that the zones of high normal displacement jumps were correlated with those where the tangential displacement jump amplitude was greater than the detection threshold [Figure 16(b)].

For the third scan, *all* nodes experienced tangential displacement jumps whose amplitude was greater than the detection threshold. Therefore, the interface was fully debonded at this stage, even though the ultimate load was not reached [Figure 4(b)]. It is interesting to note that many of the nodes still had normal displacement jumps less than the detection threshold [Figure 16(c)]. From these observations, it is concluded that interlocking was still active over the full height of the fiber. A force increment of less than 100 N led the debond zone to move from about half the fiber height down to its full height.

For the last five scans, unloading occurred in comparison to the level reached previously [Figure 4(b)]. Such phenomenon induced lower tangential and normal displacement jumps. The displacement jump activity concentrated back in the upper half of the fiber, contrary to the normal displacement jumps [Figure 16(d-h)]. Apart from the very top part of the fiber, the highest displacement jump amplitudes coincided with straight zones of the fiber. The fraction of nodes whose displacement jump was greater than the detection threshold was equal to 79%, 51%, 51%, 52%, 64%, respectively. Even though the applied load decreased from scan 05 to 08, the fraction of debonded nodes did not follow the same trend.

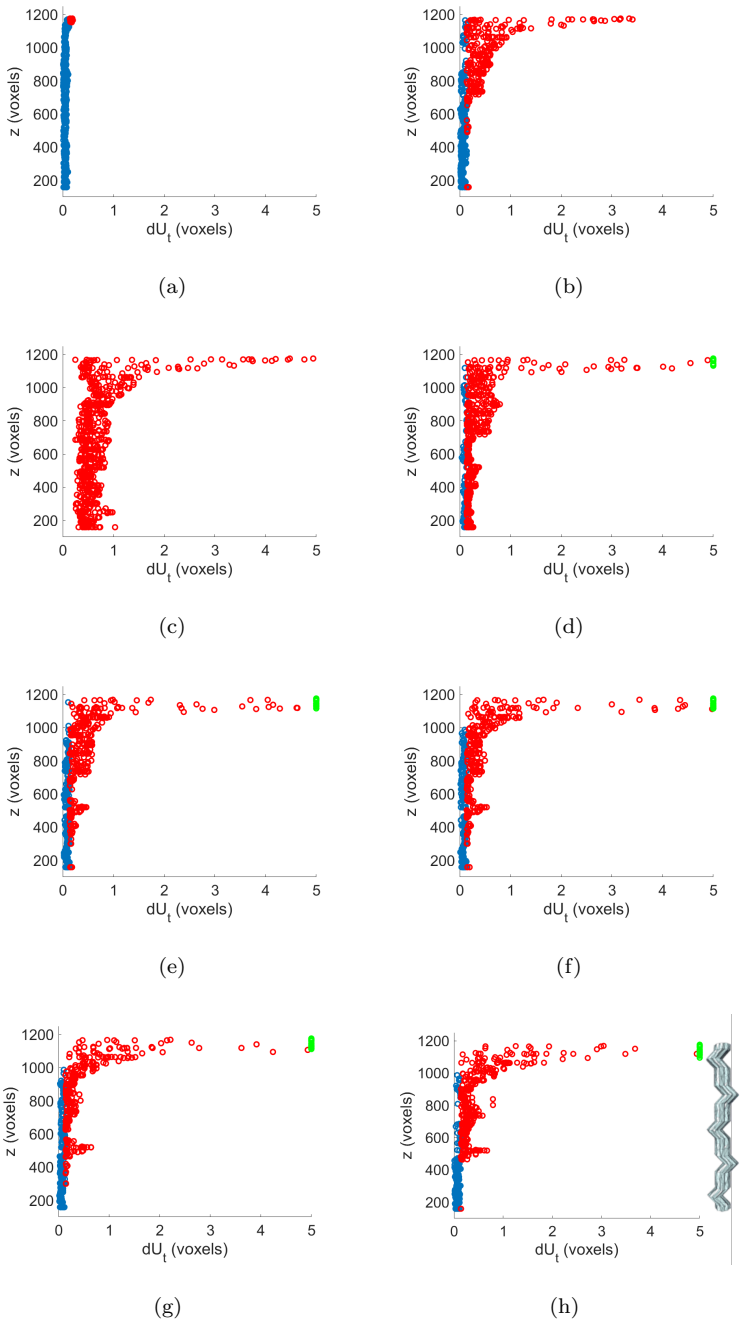

Figure 17: Norm of tangential displacement jump as a function of vertical nodal position of scans 01 (a), 02 (b), 03 (c), 04 (d), 05 (e), 06 (f), 07 (g) and 08 (h) of sample P1. Values below the detection threshold are shown in blue and above in red. Data whose level does not lie within the selected range are shown with a saturated value in green.

The general trends observed for the norm of tangential displacement jumps were close to those of the vertical displacement jumps (Figure 18). However, there were some additional features. First, once the interface was totally debonded [Figure 18(c)], negative displacement jumps occurred in the lower part of the fiber. Conversely, when the applied force decreased from scan 04 on, the displacement jumps in that same zone were lower again (and mostly non negative). In the upper part where the fiber was not aligned with the loading direction, some nodes experienced negative displacement jumps, which was induced by bending. In the other part of the fiber, the highest levels of displacement jumps coincided with straight parts of the fiber. The fraction of nodes whose displacement jump was greater than the detection threshold was less than 1% for scan 01, and equal to 37%, 56%, 42%, 42%, 41%, 41%, 48% for the next seven scans. It is interesting to note that the highest fraction was reached for scan 03 (*i.e.*, just before the peak load). This result shows that the magnitude of displacement jumps decreased after the first load drop but then stabilized and started to increase again at the very end of the test.

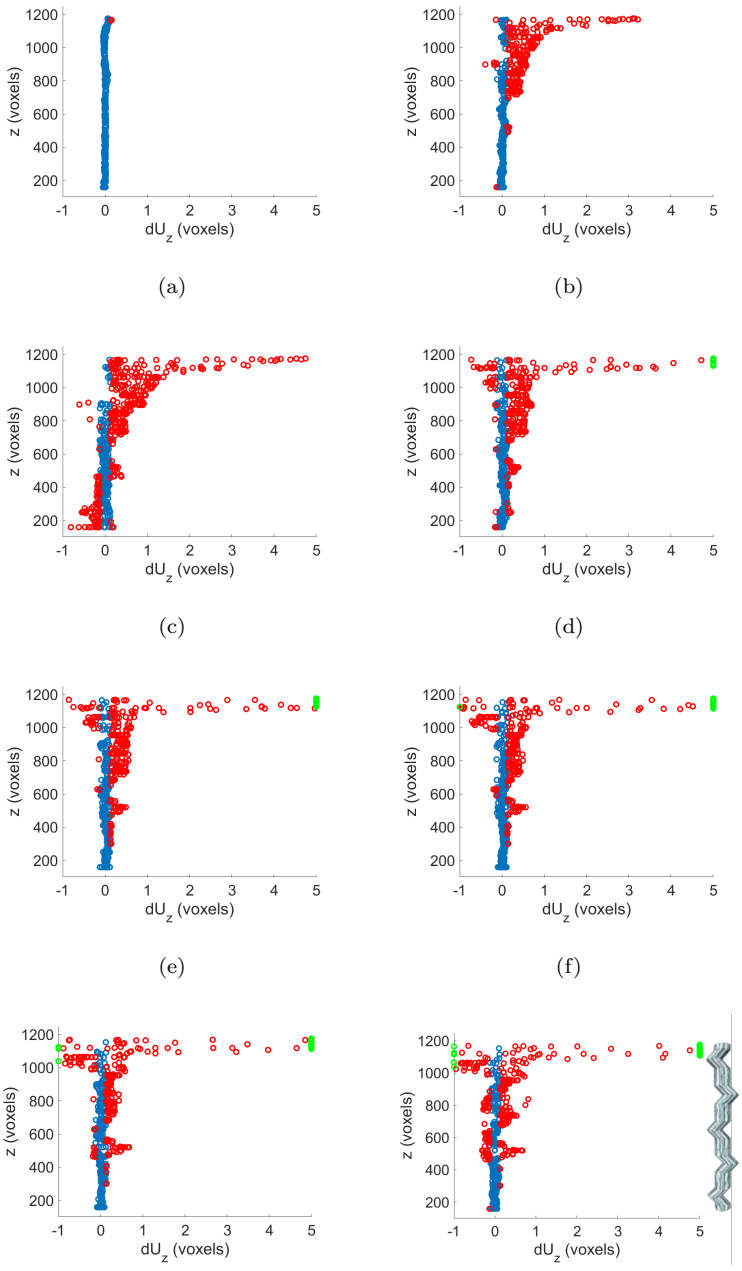

Figure 18: Vertical displacement jump as a function of vertical nodal position of scans 01 (a), 02 (b), 03 (c), 04 (d), 05 (e), 06 (f), 07 (g) and 08 (h) of sample P1. Values below the detection threshold are shown in blue and above in red. Data whose level does not lie within the selected range are shown with a saturated value in green.

The vertical strain profiles in the fiber are shown in Figure 19. Even though debonding was observed along the whole height [Figure 17], the strain fluctuations due to fiber bending remained very limited up to scan 07, except in the top part of the fiber. In the latter, the strains concentrated very early on. This part of the fiber experienced very high strains that led to fiber failure at the end of the test. It is also interesting to note that a second zone (between 400 and 600 vx) underwent more bending, which also coincided with higher tangential displacement jumps [Figure 17] (most probably due to a tensile stiffening effect [34]). At the very end of the test (*i.e.*, scan 08), the fiber was bent more significantly over about two thirds of its height.

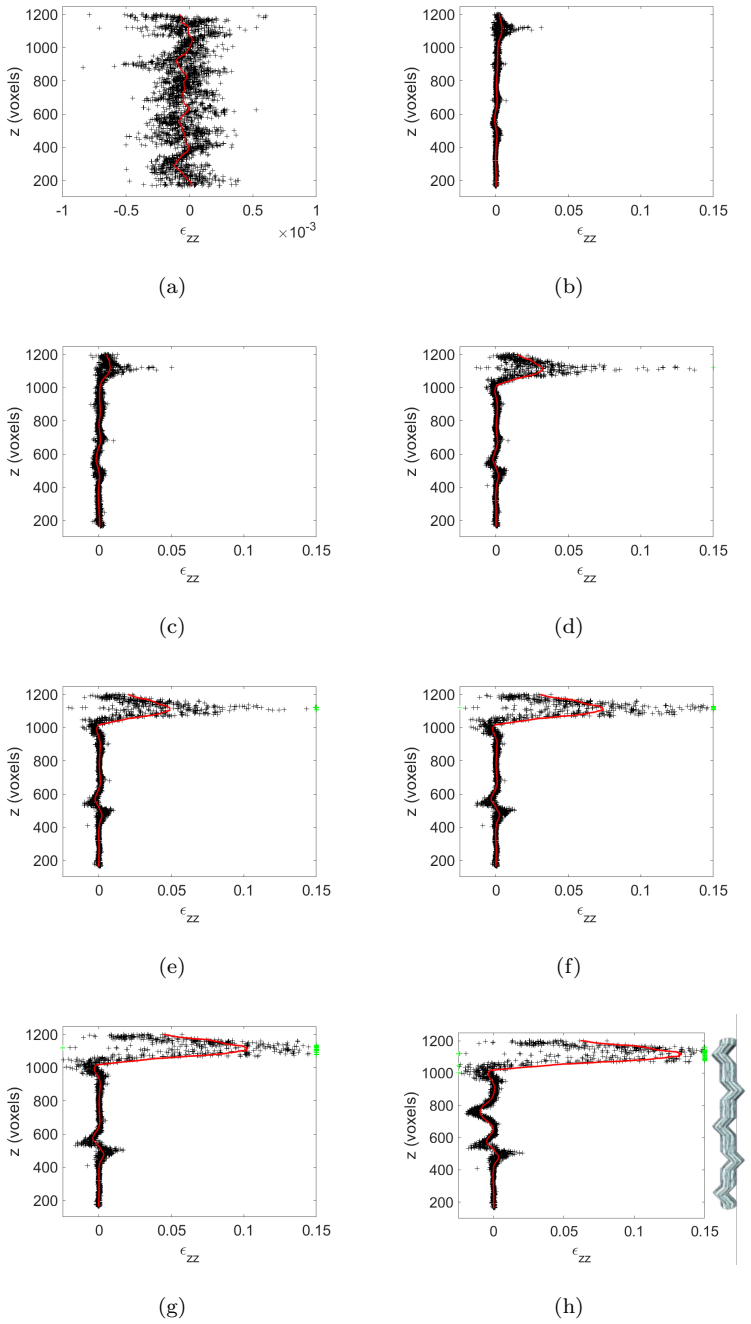

Figure 19: Vertical strain in the fiber ϵ_{zz} as a function of vertical position of element center of gravity z for scans 01 (a), 02 (b), 03 (c), 04 (d), 05 (e), 06 (f), 07 (g) and 08 (h) of sample P1. The red line depicts the k-point mean values (with $k = 100$ vx). Data whose level does not lie within the selected range are shown with a saturated value in green.

The analysis of tangential displacement jumps of test P1 showed that full debonding was achieved for the scan corresponding to the highest applied force. However, the normal displacement jumps remained very small, thereby indicating that interlocking was still active. Beyond the ultimate force, the distribution of normal displacement jumps mostly concentrated in the upper third of the fiber, that of the tangential displacement norm over two thirds of the fiber. The vertical strain profiles in the fiber confirmed the previous observations. In particular, bending remained limited except in some areas of higher debonding and at the top part of the fiber where failure took place. It is concluded that diffuse debonding of the fiber-matrix interface did not occur during the present test.

4.3. Test P2

The last in-situ test repeated the testing conditions of test P1 with a plaster matrix from the same batch and the same kind of fiber. However, as shown in Figure 4, scans were performed at different load levels and a smaller number was acquired. Figure 20 displays the normal displacement jump profiles along the vertical direction computed for sample P2. For the first scan, apart from an outlier, all measurements led to levels lower than the detection threshold. For the second scan, the displacement jumps increased, yet remained very small to deem debonding to be active except for few nodes (*i.e.*, 5%) located essentially in the upper half of the fiber.

For the third scan (*i.e.*, $F = 750$ N), the number of nodes with displacement jump amplitudes greater than their measurement uncertainties (*i.e.*, 13%) was very limited. For the last two scans, the fraction of nodes whose normal displacement jump was greater than the detection threshold was equal to 19% in both cases, which is very close to the fraction obtained for scan 03 even though the applied force was about one half the level reached in the third scan [Figure 20(c)]. The debond zone extended over the last three fiber protrusions [Figure 20(e)].

All these results show that interlocking was active in a very significant way

throughout the whole test since the normal displacement jumps remained very small. Compared to sample P1 (Figure 20), the normal displacement jumps remained significantly lower. The fraction of nodes whose displacement jump was greater than the detection threshold was less than 20% for sample P2 and reached more than 50% for sample P1. The above observations prove that debonding effects were less pronounced in the present case, as compared to test P1.

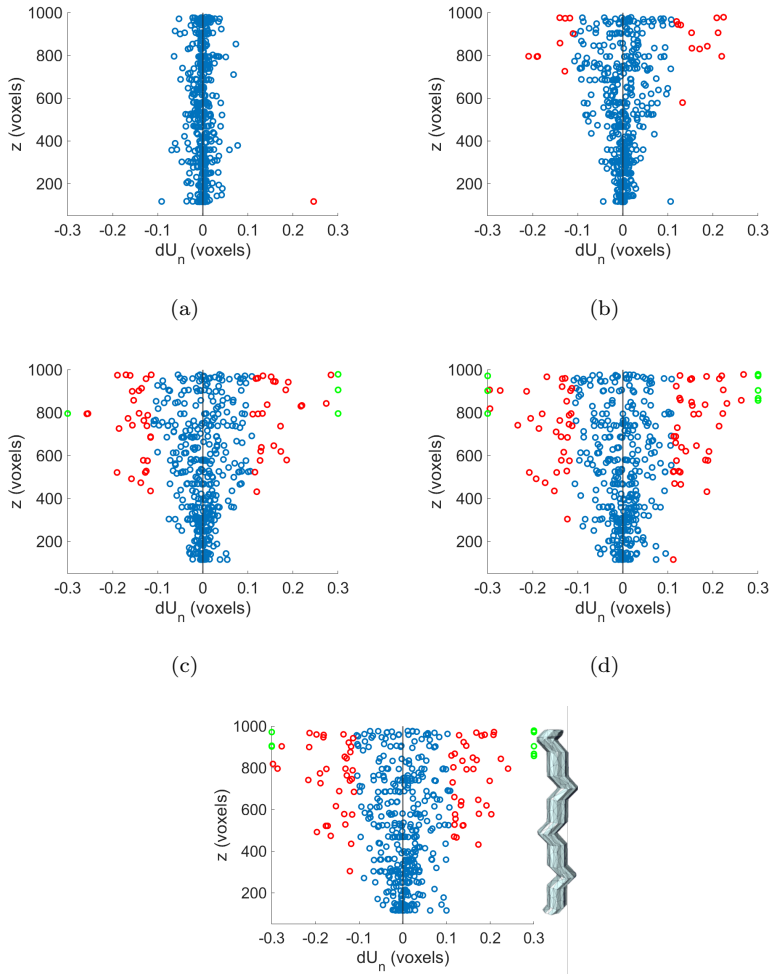

Figure 20: Normal displacement jump as a function of vertical nodal position of scans 01 (a), 02 (b), 03 (c), 04 (d) and 05 (e) of sample P2. Values below the detection threshold are shown in blue and above in red. Data whose level does not lie within the selected range are shown with a saturated value in green.

In Figure 21, the profiles of the norm of the tangential displacement jumps are shown for the five acquired scans. In the present case, the measurement uncertainties were higher (scan 01) in comparison to sample P1. For the second scan, the top half of the fiber underwent significant displacement jumps. The fraction of nodes whose displacement jump was greater than the detection threshold was equal to 31%. Such observation could not be anticipated from the normal displacement jump profiles (Figure 20). This fact further proves that interlocking was active.

For the third scan, the percentage of nodes whose displacement jump was greater than the detection threshold was equal to 39%. These nodes were essentially located in the top half of the fiber. For the last two scans, unloading occurred in comparison to the level reached previously [Figure 21(c)]. However, the tangential displacement jumps did not decrease at all. The percentage of nodes whose displacement jump was greater than the detection threshold was equal to 48% in both cases. Further, most of the interface nodes experienced normal displacements greater than the detection threshold. However, it is worth noting that the debonding activity characterized by the tangential displacement jumps developed with very limited amplitudes of normal displacements (Figure 20). As anticipated from the analysis of the normal displacement jumps, debonding extended over the last three fiber protrusions [Figure 21(e)]. Compared to sample P1, which experienced complete debonding [Figure 17(c)], it was not the case for sample P2, even though debonding was significant.

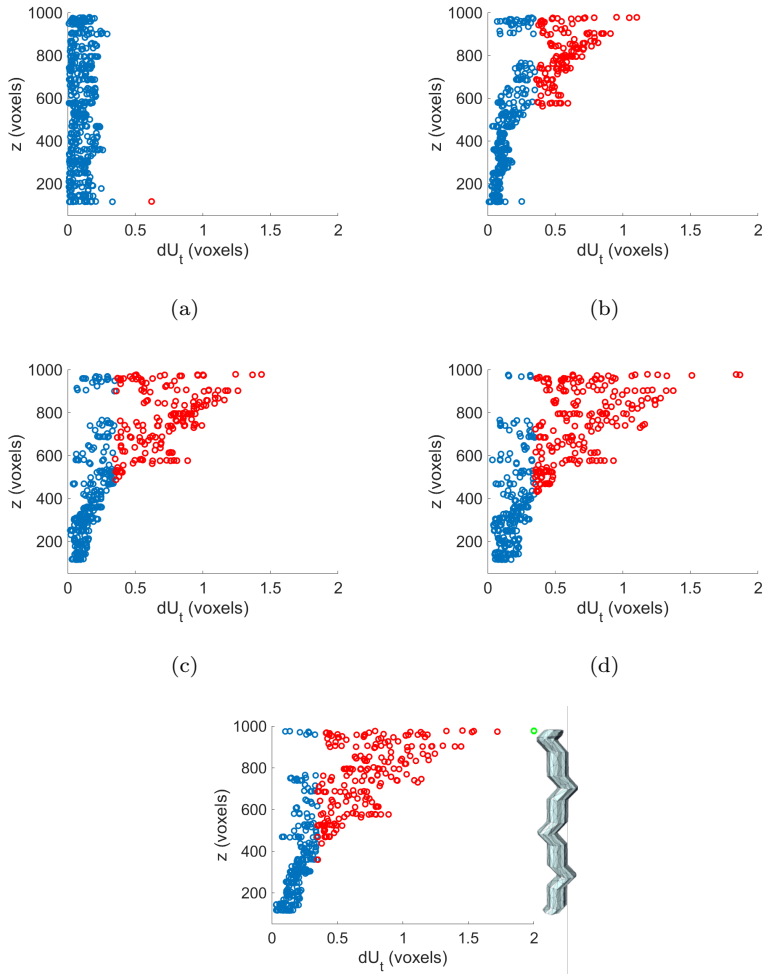

Figure 21: Norm of tangential displacement jump as a function of vertical nodal position of scans 01 (a), 02 (b), 03 (c), 04 (d) and 05 (e) of sample P2. Values below the detection threshold are shown in blue and above in red. Data whose level does not lie within the selected range are shown with a saturated value in green.

The profiles of vertical displacement jumps are shown in Figure 22. For the second scan, the top half of the fiber was debonded, as anticipated from the profiles of the tangential displacement jumps (Figure 21). The percentage of nodes whose displacement jump was greater than the detection threshold was equal to 38%. For the last three scans, it was equal to 53%, 66%, and 67%, respectively. From the profile of the third scan, it is inferred that debonding occurred almost everywhere along the fiber, in particular in vertical regions of the fiber [Figure 22(e)]. This observation also applied to scans 04 and 05.

It is worth noting that the debonding activity is more pronounced when analyzing this last displacement jump component. It is especially true for vertical portions of the fiber [Figure 22(e)] for which locking was less active. The current response is explained by diffuse shear damage of the matrix-fiber interface.

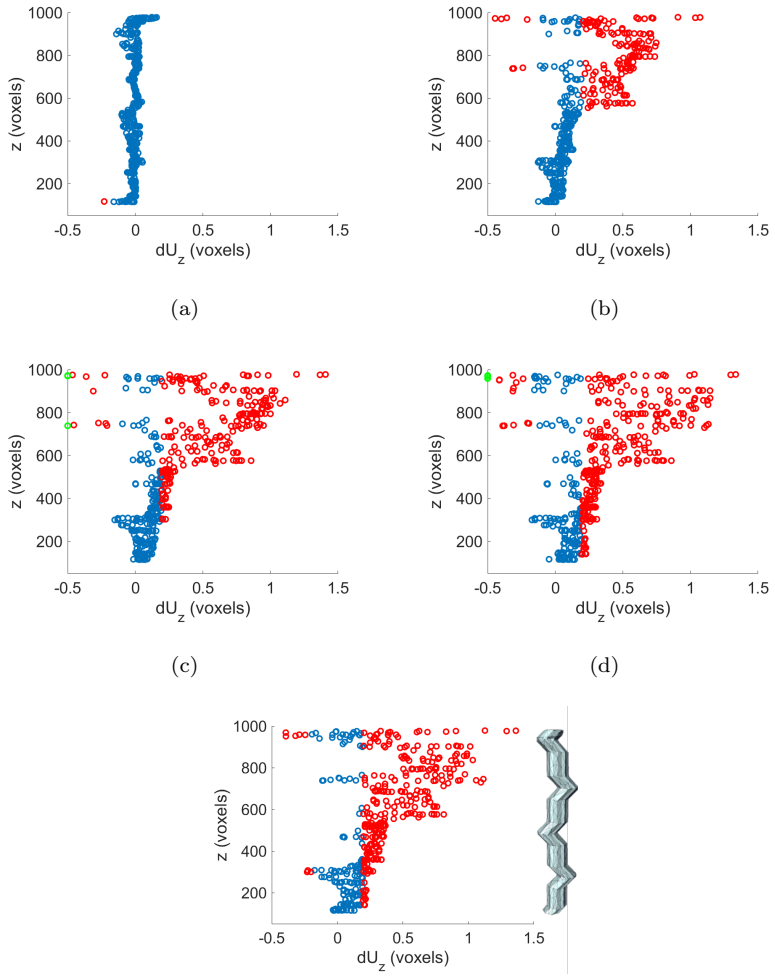

Figure 22: Vertical displacement jump as a function of vertical nodal position of scans 01 (a), 02 (b), 03 (c), 04 (d) and 05 (e) of sample P2. Values below the detection threshold are shown in blue and above in red. Data whose level does not lie within the selected range are shown with a saturated value in green.

The vertical strain profiles in the fiber are displayed in Figure 23. For the first (repeat) scan, the strain levels remained low, even though higher values were observed at both ends of the fiber [Figure 23(a)]. From scan 02 on, there are strain fluctuations in fiber that are due to its specific geometry. The fact that the strain fluctuations are correlated to the fiber morphology shows that it is fully loaded very early on. This observation is consistent with the fact that debonding occurred over a significant part of the fiber height. For scans 04 and 05, the vertical strains started concentrating on the upper part of the fiber, which are the early signs of fiber breakage. Last, bending occurred in many protrusions.

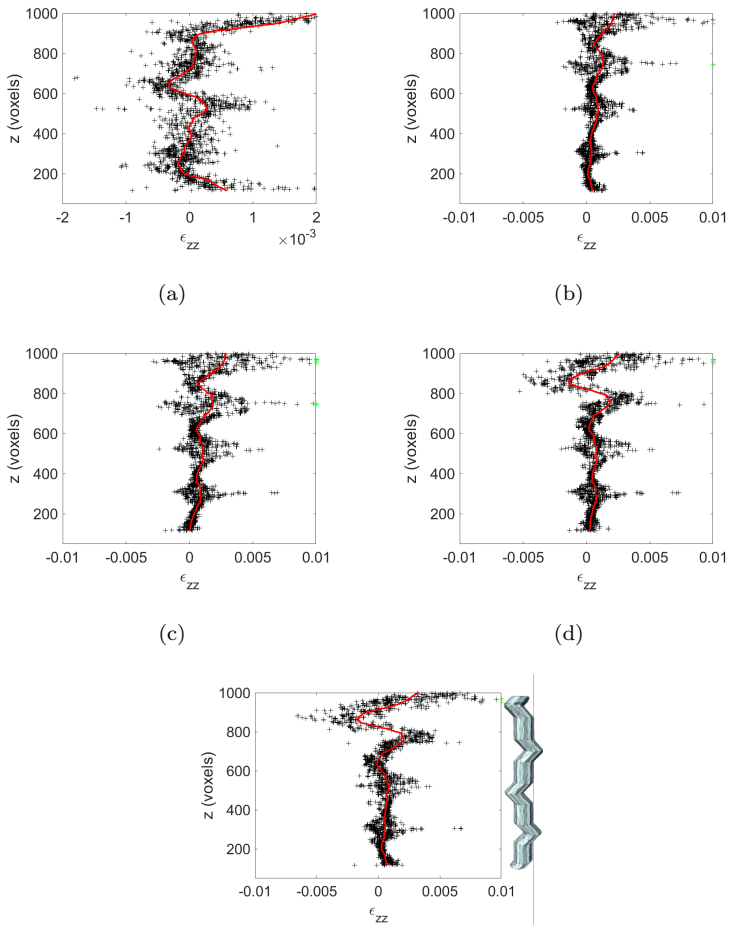

Figure 23: Vertical strain in the fiber ϵ_{zz} as a function of vertical position of element center of gravity z for scans 01 (a), 02 (b), 03 (c), 04 (d) and 05 (e) of sample P2. The red line depicts the k-point mean values (with $k = 100$ vx). Data whose level does not lie within the selected range are shown with a saturated value in green.

The analysis of the vertical displacement jumps of test P2 evidenced that debonding was reached for most of the interface for the scan corresponding to the highest applied force. However, the normal displacement jump amplitudes remained very small, thereby indicating that interlocking was still active. Beyond the ultimate force, the distribution of normal displacement jumps mostly

concentrated in the upper third of the fiber, that of the tangential displacement norm over two thirds of the fiber. The profiles of the vertical strains in the fiber showed that bending was activated very early on, contrary to the other two cases. It is concluded that interlocking forces were active in the regions comprised between the ribs, in all the examined scans.

5. Conclusion

It was shown that FE-based DVC analyses offered the opportunity to precisely analyze pull-out tests and to get access to the mechanical response of interfaces. Imaged-based meshes with split nodes at the interface between fractal fibers and brittle matrices, and independent regularization of interfacial nodes, were developed and described in the course of the present study.

This framework allowed for the characterization of interlocking and interfacial behavior during debonding by distinguishing normal, tangential and vertical displacement jumps. By performing repeated scans of the reference configurations, the measurement uncertainties were evaluated. The latter ones then served to set the detection threshold of the displacement jumps to characterize the debonding activity. It appeared on three in-situ tests that a variety of interfacial responses could occur such as debonding on the whole height or very localized debonding. The DVC analyses provided significant and discriminant information about debonding scenarios even if displacement jumps occur with small amplitudes of several voxels (*i.e.*, of the order of 100 µm). Similarly, profiles of the vertical strains showed how debonding could be understood from the fiber perspective.

The debonding mechanisms suggested that interlocking forces may be initially driven by tensile stiffening effects occurring between subsequent debonded (or cracked) regions (see, *e.g.*, Ref. [34] and references therein). Such effects were active in correspondence to the regions placed between the transverse ribs of the analyzed fibers. It was observed that fiber pull-out caused initiation of debonding and cracks in correspondence with the ribs, during the initial stages

of pull-out tests, and next more diffuse damage of the fiber-matrix interface, for larger values of the pull-out displacement.

The present experimental database may also be used to calibrate interfacial models using bulk kinematic measurements in addition to global data [14, 35], surface observations [12] or surface measurements [13]. More detailed experimental study of debonding effects are called for by considering different fractal geometries of the reinforcing fibers (*e.g.*, $n = 2$, and $m = 2$), and different matrix materials (*e.g.*, mortar and plaster with variable porosity).

6. Acknowledgement

GJ was supported by ENS Paris-Saclay International Incoming Scholarship Program and Dr. Jürgen und Irmgard Ulderup Stiftung. FF is grateful to the Italian Ministry of University and Research for support through the PRIN 2017 grant 2017J4EAYB. This work was also partially supported by the French-German Doctoral College SNTA and the French "Agence Nationale de la Recherche" through the "Investissements d'avenir" program (ANR-10-EQPX-37 MATMECA Grant).

References

[1] D. Avnir, O. Biham, D. Lidar, O. Malcai, Is the geometry of nature fractal?, Science 279 (5347) (1998) 39–40.

[2] M. M. Khoshhesab, Y. Li, Mechanical behavior of 3d printed biomimetic koch fractal contact and interlocking, Extreme Mechanics Letters 24 (2018) 58–65.

[3] Y. Li, C. Ortiz, M. C. Boyce, A generalized mechanical model for suture interfaces of arbitrary geometry, Journal of the Mechanics and Physics of Solids 61 (4) (2013) 1144–1167.

[4] L. Djumas, A. Molotnikov, G. P. Simon, Y. Estrin, Enhanced mechanical performance of bio-inspired hybrid structures utilising topological interlocking geometry, Scientific Reports 6 (2016).

[5] I. Farina, R. Goodall, E. Hernández-Nava, A. di Filippo, F. Colangelo, F. Fraternali, Design, microstructure and mechanical characterization of Ti6Al4V reinforcing elements for cement composites with fractal architecture, Materials & Design 172 (2019) 107758.

[6] I. Farina, F. Fabbrocino, G. Carpentieri, M. Modano, A. Amendola, R. Goodall, L. Feo, F. Fraternali, On the reinforcement of cement mortars through 3d printed polymeric and metallic fibers, Composites Part B: Engineering 90 (2016) 76–85.

[7] J. Li, Z. Wu, C. Huang, L. Li, Multiscale carbon nanotube-woven glass fiber reinforced cyanate ester/epoxy composites for enhanced mechanical and thermal properties, Composites Science and Technology 104 (2014) 81–88.

[8] H. Mei, Q. Bai, T. Ji, H. Li, L. Cheng, Effect of carbon nanotubes electrophoretically-deposited on reinforcing carbon fibers on the strength and toughness of c/sic composites, Composites Science and Technology 103 (2014) 94–99.

[9] M.-W. Moon, A. Vaziri, Surface modification of polymers using a multi-step plasma treatment, Scripta Materialia 60 (1) (2009) 44–47.

[10] X. Zheng, H. Lee, T. H. Weisgraber, M. Shusteff, J. DeOtte, E. B. Duoss, J. D. Kuntz, M. M. Biener, Q. Ge, J. A. Jackson, S. O. Kucheyev, N. X. Fang, C. M. Spadaccini, Ultralight, ultrastiff mechanical metamaterials, Science 344 (6190) (2014) 1373–1377.

[11] RILEM TC, AAC 8.1 Pull-out test for reinforcement, 1992, in: RILEM Recommendations for the Testing and Use of Constructions Materials, E & FN SPON, 1994, p. 140.

[12] A. Vervuurt, J. Van Mier, E. Schlangen, Analyses of anchor pull-out in concrete, Materials and Structures 27 (5) (1994) 251–259.

[13] A. Ouglova, Y. Berthaud, F. Foct, M. François, F. Ragueneau, I. Petre-Lazar, The influence of corrosion on bond properties between concrete and reinforcement in concrete structures., Materials and Structures 41 (2008) 969–980.

[14] F. Greco, L. Leonetti, R. Luciano, A multiscale model for the numerical simulation of the anchor bolt pull-out test in lightweight aggregate concrete, Construction and Building Materials 95 (2015) 860–874.

[15] A. Qasem, Y. Sallam, H. Eldien, B. Ahangarn, Bond-slip behavior between ultra-high-performance concrete and carbon fiber reinforced polymer bars using a pull-out test and numerical modelling, Construction and Building Materials 260 (2020) 119857.

[16] E. Maire, P. J. Withers, Quantitative X-ray tomography, International Materials Reviews 59 (1) (2014) 1–43.

[17] J. Buffière, E. Maire, J. Adrien, J. Masse, E. Boller, In Situ Experiments with X ray Tomography: an Attractive Tool for Experimental Mechanics, Experimental Mechanics 50 (3) (2010) 289–305.

[18] B. Bay, T. Smith, D. Fyhrie, M. Saad, Digital volume correlation: three-dimensional strain mapping using X-ray tomography, Experimental Mechanics 39 (1999) 217–226.

[19] B. Bay, Methods and applications of digital volume correlation, Journal of Strain Analysis for Engineering Design 43 (2008) 745–760.

[20] A. Buljac, C. Jailin, A. Mendoza, J. Neggers, T. Taillandier-Thomas, A. Bouterf, B. Smaniotto, F. Hild, S. Roux, Digital Volume Correlation: Review of Progress and Challenges, Experimental Mechanics 58 (5) (2018) 661–708.

[21] T. Oesch, In-situ CT investigation of pull-out failure for reinforcing bars embedded in conventional and high-performance concretes, in: 6th Conference on Industrial Computed Tomography, 2016.

[22] M. D. Smedt, K. D. Wilder, E. Verstrynge, L. Vandewalle, Experimental Analysis of Monotonic and Cyclic Pull-Out of Steel Fibres by Means of Acoustic Emission and X-ray Microfocus Computed Tomography, Proceedings 2 (8) (2018) 396.

[23] M. Flansbjer, N. W. Portal, S. Hall, J. Engqvist, Analysis of Failure Modes in Fiber Reinforced Concrete Using X-ray Tomography and Digital Volume Correlation, Proceedings 2 (8) (2018).

[24] A. Buljac, M. Shakoor, M. Bernacki, P.-O. Bouchard, T. Morgeneyer, F. Hild, Numerical validation framework for micromechanical simulations based on synchrotron 3D imaging, Computational Mechanics 59 (3) (2017) 419–441.

[25] A. Tsitova, F. Bernachy-Barbe, B. Bary, S. Al Dandachli, C. Bourcier, B. Smaniotto, F. Hild, Damage Quantification via Digital Volume Correlation with Heterogeneous Mechanical Regularization: Application to an In Situ Meso-Flexural Test on Mortar, Experimental Mechanics 62 (2022) 333–349.

[26] F. Hild, A. Bouterf, S. Roux, Damage Measurements via DIC, International Journal of Fracture 191 (1-2) (2015) 77–105.

[27] T. Taillandier-Thomas, S. Roux, T. Morgeneyer, F. Hild, Localized strain field measurement on laminography data with mechanical regularization, Nuclear Instruments and Methods in Physics Research Section B 324 (2014) 70–79.

[28] A. Mendoza, J. Neggers, F. Hild, S. Roux, Complete Mechanical Regularization Applied to Digital Image and Volume Correlation, Computer Methods in Applied Mechanics and Engineering 355 (2019) 27–43.

[29] M. Reuter, S. Biasotti, D. Giorgi, G. Patanè, M. Spagnuolo, Discrete Laplace–Beltrami operators for shape analysis and segmentation, Computers & Graphics 33 (3) (2009) 381–390.

[30] H. Leclerc, J. Périé, S. Roux, F. Hild, Voxel-scale digital volume correlation, Experimental Mechanics 51 (4) (2011) 479–490.

[31] H. Leclerc, J. Neggers, F. Mathieu, F. Hild, S. Roux, Correli 3.0, IDDN.FR.001.520008.000.S.P.2015.000.31500, Agence pour la Protection des Programmes, Paris (France) (2015).

[32] ISO, Guide to the Expression of Uncertainty in Measurements (GUM), International Organization for Standardization, Geneva (Switzerland), 1995.

[33] A. Buljac, T. Taillandier-Thomas, L. Helfen, T. Morgeneyer, F. Hild, Evaluation of measurement uncertainties of digital volume correlation applied to laminography data, Journal of Strain Analysis for Engineering Design 53 (2018) 49–65.

[34] M. Islam, Investigation of long-term tension stiffening mechanism for ultra-high-performance fiber reinforced concrete (UHPFRC), Construction and Building Materials 321 (2022) 126310.

[35] U. De Maio, N. Fantuzzi, F. Greco, L. Leonetti, A. Pranno, Failure Analysis of Ultra High-Performance Fiber-Reinforced Concrete Structures Enhanced with Nanomaterials by Using a Diffuse Cohesive Interface Approach, Nanomaterials 10 (9) (2020) 1792.

[36] F. Hild, A. Bouterf, L. Chamoin, F. Mathieu, J. Neggers, F. Pled, Z. Tomičević, S. Roux, Toward 4D Mechanical Correlation, Advanced Modeling and Simulation in Engineering Sciences 3 (1) (2016) 1–26.

7. Appendix: DVC Hardware and Analysis Parameters

Table 2: DVC hardware parameters

Tomograph	North Star Imaging X50+
X-ray source	XRayWorX XWT-240-CT
Target / Anode	32.5 W (reflection mode)
Filter	none
Voltage	180 kV
Current	200 µA
Focal spot size	5 µm
Tube to detector	496 mm
Tube to object	153 mm
Detector	Dexela 2923
Definition	1536×1944 pixels (2×2 binning)
Number of projections	1000
Angular amplitude	360°
Frame average	10 per projection
Frame rate	20 fps
Acquisition duration	around 20 min
Reconstruction algorithm	filtered back-projection
Gray Levels amplitude	16 bits
Volume size	$880 \times 871 \times 1148$ voxels (after crop)
Field of view	$88.0 \times 87.1 \times 114.8$ mm^3 (after crop)
Image scale	46 µm/voxel

Table 3: DVC analysis parameters

DVC software	Correli 3.0 [31]
Image filtering	none
Element length (mean)	46 vx
Shape functions	linear (T4 elements) [36]
Mesh	see Figure 5
Matching criterion	penalized sum of squared differences
Regularization length bulk	$\ell_{reg} = 50$ vx
Regularization length interface	$\ell_{reg}^{int} = 50\sqrt{2}$ vx
Interpolant	cubic